The Astrophysical Journal, 832:175 (13pp), 2016 December 1 doi:10.3847/0004-637X/832/2/175

EXPLORING DAMPED Lyα SYSTEM HOST GALAXIES USING GAMMA-RAY BURSTS

Vicki L. Toy[1], Antonino Cucchiara[2,3,4], Sylvain Veilleux[1,5], Michele Fumagalli[6], Marc Rafelski[2,3,8], Alireza Rahmati[7], S. Bradley Cenko[2,5], John I. Capone[1], and Dheeraj R. Pasham[2,5]
[1] Department of Astronomy, University of Maryland, College Park, MD 20742, USA
[2] NASA, Goddard Space Flight Center, Greenbelt, MD 20771, USA
[3] Space Telescope Science Institute, Baltimore, MD 21218, USA
[4] University of the Virgin Islands, College of Science and Mathematics, #2 John Brewers Bay, 00802 St. Thomas, VI, USA
[5] Joint Space-Science Institute, University of Maryland, College Park, MD 20742, USA
[6] Institute for Computational Cosmology and Centre for Extragalactic Astronomy, Department of Physics, Durham University, South Road, Durham DH1 3LE, UK
[7] Institute for Computational Science, University of Zürich, Winterthurerstrasse 190, CH-8057 Zürich, Switzerland
Received 2016 June 13; revised 2016 August 29; accepted 2016 September 15; published 2016 November 30

ABSTRACT

We present a sample of 45 Damped Lyα system (DLA; $N_{\rm H\,I} \geqslant 2 \times 10^{20}\,{\rm cm}^{-2}$) counterparts (33 detections, 12 upper limits) which host gamma-ray bursts (GRB-DLAs) in order to investigate star formation and metallicity within galaxies hosting DLAs. Our sample spans $z \sim 2$–6 and is nearly three times larger than any previously detected DLA counterparts survey based on quasar line-of-sight searches (QSO-DLAs). We report star formation rates (SFRs) from rest-frame UV photometry and spectral energy distribution modeling. We find that DLA counterpart SFRs are not correlated with either redshift or H I column density. Thanks to the combination of *Hubble Space Telescope* and ground-based observations, we also investigate DLA host star formation efficiency. Our GRB-DLA counterpart sample spans both higher efficiency and low efficiency star formation regions compared to the local Kennicutt–Schmidt relation, local star formation laws, and $z \sim 3$ cosmological simulations. We also compare the depletion times of our DLA hosts sample to other objects in the local universe; our sample appears to deviate from the star formation efficiencies measured in local spiral and dwarf galaxies. Furthermore, we find similar efficiencies as local inner disks, SMC, and Lyman-break galaxy outskirts. Finally, our enrichment time measurements show a spread of systems with under- and over-abundance of metals, which may suggest that these systems had episodic star formation and a metal enrichment/depletion as a result of strong stellar feedback and/or metal inflow/outflow.

Key words: galaxies: high-redshift – galaxies: ISM – galaxies: star formation – gamma-ray burst: general – ISM: atoms

1. INTRODUCTION

There are several successful methods to identify galaxies in the early universe. For example, Lyman-break galaxies (LBGs; Steidel et al. 1996) are found using the photometric drop-out technique around the Lyman-limit and have provided the first sample of $z \gtrsim 8$ galaxies (e.g., Bouwens et al. 2010; Oesch et al. 2012). Lyα emitters (LAE), in which hydrogen recombines after ionization by young stars, are identified at the highest redshifts with deep near-infrared observing campaigns ($z \sim 7.7$; Hibon et al. 2010; Tilvi et al. 2010; Krug et al. 2012). Because the Lyα (Lyα) line is less sensitive to the overall stellar continuum, LAEs are generally lower mass systems with negligible dust (Gawiser et al. 2007; Guaita et al. 2011). Additionally, millimeter/submillimeter observations have opened a promising way to study galaxies at $z \gtrsim 1$ through CO molecular emission at high redshift (e.g., Daddi et al. 2009). These methods mainly probe the bright end of the luminosity function, at least at the highest redshifts, due to their strong stellar UV continuum.

Another method to identify high-redshift galaxies, while also characterizing their chemical enrichment, utilizes bright background objects like high-redshift quasars (QSO), gamma-ray burst (GRB) afterglows, or, even more recently, extended background galaxies (Cooke & O'Meara 2015; Mawatari et al. 2016) to identify absorption-line systems. These detections depend only on the gas cross-section and therefore are less sensitive to the luminosity of the associated object (an observing bias that affects every high-redshift galaxy survey). Specifically, diffuse gaseous clouds in the universe are primarily described by their neutral hydrogen column density ($N_{\rm H\,I}$). Recent surveys have demonstrated that Damped Lyα systems (DLAs, see Wolfe et al. 2005), characterized by $N_{\rm H\,I} \geqslant 2 \times 10^{20}\,{\rm cm}^{-2}$, contain ⩾80% of the neutral gas available for star formation (Péroux et al. 2003; Prochaska et al. 2005; Prochaska & Wolfe 2009; Noterdaeme et al. 2009, 2012b; Zafar et al. 2013). At $z = 2$–3, they contain enough gas to account for a significant fraction (20%–50%) of stellar mass in all galaxies (Storrie-Lombardi & Wolfe 2000; Wolfire et al. 2003; O'Meara et al. 2007). Most importantly, they provide a powerful independent check on sophisticated models of galaxy formation, which also include the effects of stellar and supernovae feedback (e.g., Bird et al. 2014; Rahmati et al. 2015).

Some suggested scenarios to explain the nature of high-redshift DLA galaxies include rapidly rotating proto-galactic disks (Prochaska & Wolfe 1997; Wolfe & Prochaska 1998; Genzel et al. 2006; Förster Schreiber et al. 2009), low surface brightness galaxies (Jimenez et al. 1999), faint and small gas-rich dwarf galaxies (Tyson 1988), compact galaxies (Nagamine et al. 2007), dwarf irregulars (Dessauges-Zavadsky et al. 2007), or gaseous halos of Lyman-break galaxies (Fynbo et al. 1999; Møller et al. 2002). There is a general consensus that the major contribution to the DLA population at $z \sim 3$ comes from halos with virial masses of $10^{10-12} M_{\odot}$ (Cooke et al. 2006; Barnes &

[8] NASA Postdoctoral Program Fellow.

Haehnelt 2009; Font-Ribera et al. 2012). Also, Rahmati & Schaye (2014) found that most DLAs at those redshifts are hosted by halos with masses around or less than $10^{10} M_{\odot}$ (see the top-right panel of Figure 6 in that paper) and, more recently, Srianand et al. (2016) suggested a predominant contribution, at high-redshift, of DLAs that are more compact than modern disk galaxies.

To understand both the nature and evolution of the DLA population it becomes critical to identify and characterize the galaxies associated with DLAs, e.g., measuring their stellar mass, metallicity, size, and star formation. Understanding the types of galaxies DLAs represent will allow us to constrain which models better describe the DLA population. There are thousands of DLAs identified from absorption-line studies, thanks to the Sloan Digital Sky Survey (SDSS) (Eisenstein et al. 2011) and the BOSS surveys (Dawson et al. 2013). We can measure the neutral gas and metal content from absorption lines, however, finding the DLA host galaxies that actually produced the identified features has been difficult, particularly at high redshift and/or at small impact parameters.

Thus far, there have only been 13 QSO-DLA confirmed galaxy counterparts. This small sample spans redshifts of $z \sim 0.9$–3.4 and impact parameters of ∼1–25 kpc (Møller & Warren 1993; Møller et al. 2002; Weatherley et al. 2005; Fynbo et al. 2011; Krogager et al. 2012; Noterdaeme et al. 2012a; Péroux et al. 2012, 2016; Bouché et al. 2013; Jorgenson & Wolfe 2014). The majority of these DLA galaxies were found by taking spectra with multiple slit overlays. This method has been successful but suffers from a strong bias toward small impact parameters because this is where most of the slits overlap. Moreover, the bright QSO precludes exploration at very small impact parameters. It is difficult to quantify selection biases with this method as non-detection statistics are not reported. Another interesting possibility is to use the Atacama Large Millimeter/submillimeter Array (ALMA) to map out CO in QSO-DLAs. Neeleman et al. (2016) successfully detected molecular emission from a galaxy along the projected background of a quasar with ALMA.

An independent method to identify host galaxies is the double-DLA method where a second DLA system along the line-of-sight of the QSO-DLA acts as a blue filter for the QSO (O'Meara et al. 2006). This method has been successful in placing limits on star formation rates (SFRs) but has so far yielded few detections (Fumagalli et al. 2015).

Finally, one can target DLAs that are identified *within GRB host galaxies* (GRB-DLAs): GRBs are extremely bright sources and can be seen up to $z \sim 9$ (Salvaterra et al. 2009; Tanvir et al. 2009; Cucchiara et al. 2011). Their bright afterglows enable the identification of the Lyα profile (which provides accurate H I column density measurement) as well as metal lines at the same redshift of the GRB host (different with respect to QSOs, where the DLA is usually at lower-redshift). There are three key advantages of using GRB- DLAs: (1) GRBs are very bright sources, providing exquisite high signal-to-noise ratio spectra even at the highest redshifts; (2) the simple power-law continuum of the afterglow emission simplifies line identification and line profile fitting with respect to the more complex QSO underlying emission; (3) the afterglow emission fades away after a few days of the explosion, enabling *direct* imaging galaxies at small impact parameters ($\lesssim 1-3$ kpc, as shown by Blanchard et al. 2016), which are often identified as the GRB host galaxies. Schulze et al. (2012) demonstrated this method with a dedicated campaign to identify the galaxy counterparts for GRB-DLAs and sub-DLAs at $z = 2$–3.6. The authors successfully detected a GRB-DLA counterpart for GRB 070721B.

The main drawback with this method is that the transient nature of GRBs often makes it difficult to obtain spectra before the GRB afterglow has faded. Consequently, it is challenging to assemble a large sample of GRB-DLAs; however, Cucchiara et al. (2015) has reported a sample of 76 confirmed GRB-DLAs and GRB sub-DLAs (for which $\log N_{\rm H\,I} < 20.3$). In the following sections, we will use this sample as a starting point to identify and characterize the galaxy counterparts of these DLAs and sub-DLAs. Our compilation represents a factor of $\gtrsim 3$ increase in the number of identified DLA galaxies to date.

The paper is divided as follows: in Section 2, we describe the GRB-DLA sample and how it compares to other GRB hosts or QSO-DLA samples; in Section 3.1, we report SFRs and stellar masses from our GRB-DLA counterparts and investigate if there is any correlation between SFR and either redshift or H I column density; in Section 3.2, we examine the relationship between SFR surface density and H I gas surface density to try to understand how star formation efficiency changes with redshift and metallicity and we compare our star formation efficiencies with galaxies in the local universe; in Section 4, we report enrichment times to understand how metals are formed in these counterparts; and, in Section 5, we summarize our results.

Throughout this paper we assume a ΛCDM model with $H_0 = 69.6$ km s^{-1} Mpc^{-1}, $\Omega_m = 0.286$, and $\Omega_\Lambda = 0.714$ (Bennett et al. 2014). All magnitudes are in the AB system (Oke & Gunn 1983) and quoted uncertainties are 1σ (68%) confidence intervals unless otherwise noted.

2. SAMPLE AND DATA REDUCTION

2.1. Sample

We use the GRB-DLA sample described in Cucchiara et al. (2015) as a starting point for our search for GRB-DLA counterparts.This sample is comprised of 76 GRB host galaxies: 59 confirmed GRB-DLAs and the remaining 17 objects are either GRB sub-DLAs or they only have either upper or lower limits on $N_{\rm H\,I}$ (the latter are likely sub-DLAs or Lyman-limit systems). We conduct a literature search for photometric observations of each associated GRB host galaxy (see Table 1 for individual observation references) and supplement these observations with data from the Large Monolithic Imager (LMI) on the Discovery Channel Telescope (DCT). All of the magnitudes are converted to AB magnitudes using Blanton & Roweis (2007) and are corrected for Galactic extinction using the dust map from Schlafly & Finkbeiner (2011). The photometry of the host galaxies is taken weeks after the GRB trigger to ensure that the GRB afterglow contribution is negligible. The majority of our sample is too faint to detect spectral emission lines; however, Blanchard et al. (2016) performed a statistical analysis of 105 long GRBs with deep *Hubble Space Telescope* (*HST*) imaging with $1''$ positioning and found that 90% of long GRBs have physical offsets of $\lesssim 5$ kpc, which makes chance associations of our sample improbable. Additionally, one expects $\lesssim 0.5$ DLA (Noterdaeme et al. 2012b; Crighton et al. 2015) and ∼1 Lyman-limit system (Prochaska et al. 2010; Ribaudo et al. 2011; Fumagalli et al. 2013; O'Meara et al. 2013) per line-of-sight at

Table 1
GRB-DLAs

GRB-DLA	Redshift[a]	$\log N_{\rm H\,I}$ ($\rm cm^{-2}$)	$\log Z/Z_\odot$	A_V	SFR[b] ($M_\odot$ $\rm yr^{-1}$)	$\log M_*$ ($M_\odot$)	$\log M_{\rm dust}$ ($M_\odot$)	References
000926	2.03621	21.30 ± 0.25	>-0.30	0.038	$3.03^{+0.97}_{-0.36}$	$9.90^{+0.16}_{-0.22}$	$6.00^{+0.55}_{-0.00}$	(1)
011211	2.1427	20.40 ± 0.20	>-1.22	0.138	$3.86^{+2.85}_{-1.00}$	$8.94^{+0.18}_{-0.28}$	$6.19^{+0.70}_{-0.19}$	(2)
020124	3.198	21.70 ± 0.20	...	0.280 ± 0.330[c]	<0.35	...	...	(3), (4)
030226	1.98	20.50 ± 0.30	>-1.28	0.060 ± 0.060[c]	<2.08	...	...	(4), (5)
030323	3.3714	21.90 ± 0.07	>-1.32	<0.020[c]	<0.69	...	...	(3), (4)
030429	2.658	21.60 ± 0.20	>-1.13	0.400 ± 0.100[c]	$3.82^{+0.79}_{-0.56}$[d]	...	...	(3), (4)
050319	3.24	20.90 ± 0.20	>-0.77	0.050 ± 0.060[c]	$2.05^{+1.14}_{-0.54}$[d]	...	...	(6), (7)
050401	2.899	22.60 ± 0.30	>-1.07	0.738	$9.16^{+11.35}_{-4.52}$	$9.56^{+0.23}_{-0.21}$	$7.00^{+0.64}_{-0.63}$	(3), (6), (8), (9)
050730	3.96723	22.10 ± 0.10	-1.96 ± 0.11	0.120 ± 0.020[c]	<0.54	...	...	(9), (10)
050820A	2.6145	21.10 ± 0.10	-0.78 ± 0.11	0.813	$8.17^{+6.19}_{-3.57}$	$9.16^{+0.17}_{-0.17}$	$6.94^{+0.60}_{-0.59}$	(3), (6), (8), (9)
050904	6.26	21.30 ± 0.20	>-1.00	<0.050[c]	<0.64[d]	...	...	(11), (12)
050922C	2.1996	21.55 ± 0.10	-1.88 ± 0.14	0.090 ± 0.030[c]	<1.23	...	...	(3), (13)
060115	3.533	21.50 ± 0.10	>-1.53	0.763	$5.85^{+8.02}_{-2.98}$	$9.33^{+0.20}_{-0.28}$	$6.81^{+0.64}_{-0.65}$	(6), (8), (9)
060206	4.048	20.85 ± 0.10	>-0.74	<0.170[c]	<0.77	...	...	(9), (13)
060210	3.913	21.55 ± 0.15	>-0.83	0.363	$51.52^{+27.36}_{-22.21}$	$9.99^{+0.15}_{-0.12}$	$7.52^{+0.61}_{-0.65}$	(6), (14)
060223A	4.41	21.60 ± 0.10	>-1.80	...	$1.03^{+0.24}_{-0.16}$[d]	...	...	(9)
060510B	4.94	21.30 ± 0.10	>-0.84	<0.500[c]	<2.23[d]	...	...	(6), (14)
060522	5.11	21.00 ± 0.30	...	...	<2.96	...	...	(15)
060707	3.425	21.00 ± 0.20	>-1.69	0.080 ± 0.020[c]	$6.54^{+0.37}_{-0.35}$	...	...	(8), (10)
060714	2.711	21.80 ± 0.10	>-0.97	0.210 ± 0.020[c]	$1.40^{+0.41}_{-0.32}$	...	...	(8), (10)
060926	3.206	22.60 ± 0.15	>-1.32	0.320 ± 0.020[c]	$6.31^{+3.52}_{-1.67}$[d]	...	...	(10), (16)
060927	5.464	22.50 ± 0.15	>-1.55	<0.170[c]	<0.32	...	...	(9), (13)
061110B	3.433	22.35 ± 0.10	>-1.84	0.230 ± 0.030[c]	$4.46^{+1.37}_{-1.05}$	...	...	(8), (10)
070110	2.351	21.70 ± 0.10	>-1.32	0.100 ± 0.100[c]	$3.43^{+0.63}_{-0.46}$[d]	...	...	(8), (10)
070506	2.308	22.00 ± 0.30	>-0.65	0.440 ± 0.050[c]	$5.09^{+0.98}_{-0.71}$[d]	...	...	(8), (10)
070721B	3.628	21.50 ± 0.20	>-2.14	0.200 ± 0.020[c]	$1.17^{+0.59}_{-0.39}$	...	...	(8), (10)
070802	2.455	21.50 ± 0.20	>-0.54	0.838	$23.28^{+26.49}_{-13.12}$	$9.71^{+0.11}_{-0.11}$	$7.33^{+0.65}_{-0.67}$	(8), (9), (17), (18)
080210	2.641	21.90 ± 0.10	>-1.37	0.330 ± 0.030[c]	$5.53^{+1.96}_{-1.45}$	...	...	(5), (10)
080607	3.037	22.70 ± 0.15	>-1.72	2.938	$116.68^{+0.00}_{-0.00}$	$10.13^{+0.00}_{-0.00}$	$8.36^{+0.49}_{-0.52}$	(6), (9), (17)
080804	2.20542	21.30 ± 0.10	-0.75 ± 0.16	0.170 ± 0.110[c]	$0.82^{+0.54}_{-0.23}$[d]	...	...	(6), (13)
081008	1.96	21.59 ± 0.10	-0.86 ± 0.14	0.290 ± 0.070[c]	$4.64^{+1.27}_{-0.82}$[d]	...	...	(7), (9)
090205	4.64	20.73 ± 0.05	>-0.57	...	$6.14^{+0.59}_{-0.54}$	...	...	(19)
090516	4.109	21.73 ± 0.10	>-1.36	...	$5.87^{+3.43}_{-2.17}$	...	...	(20)
090812	2.425	22.30 ± 0.10	>-1.64	0.230 ± 0.080[c]	<561.26	...	...	(5), (13)
100219A	4.667	21.13 ± 0.12	-0.95 ± 0.18	0.130 ± 0.050[c]	$5.45^{+1.89}_{-1.12}$[d]	...	...	(21)
110205A	2.214	21.45 ± 0.20	>-0.82	0.350 ± 0.060[c]	$2.65^{+1.74}_{-0.75}$[d]	...	...	(6), (13)
111008A	4.98968	22.30 ± 0.06	-1.63 ± 0.13	0.110 ± 0.040[c]	<7.16	...	...	(22)
120327A	2.813	22.01 ± 0.09	-1.51 ± 0.11	<0.030[c]	<14.16	...	...	(23)
120716A	2.487	21.55 ± 0.15	>-1.76	...	<2.84	...	...	(5)
120909A	3.9293	21.20 ± 0.10	-0.66 ± 0.11	...	$3.31^{+0.39}_{-0.35}$	...	...	(20)
121024A	2.2977	21.50 ± 0.10	-0.40 ± 0.12	0.563	$36.90^{+32.60}_{-16.39}$	$10.15^{+0.16}_{-0.17}$	$7.54^{+0.60}_{-0.60}$	(24)
121201A	3.385	21.70 ± 0.20	...	...	$6.45^{+1.38}_{-1.13}$	...	...	(20)
130408A	3.757	21.70 ± 0.10	-1.24 ± 0.12	...	<6.54	...	...	(20)
130505A	2.2687	20.65 ± 0.10	>-1.42	<0.128[c]	<7.47	...	...	(5), (25)
140423A	3.258	20.45 ± 0.20	>-1.44	...	<8.95	...	...	(5)

Notes.
[a] Significant digits of redshift reflect accuracy of measurement.
[b] Dust-corrected (except those without A_V measurements).
[c] Host extinction from GRB afterglow measurements.
[d] Calculates SFR from MAGPHYS SED scaling of photometric detection. (1) Castro et al. (2003), (2) Fynbo et al. (2003), (3) Chen et al. (2009), (4) Kann et al. (2006), (5) This work, (6) Perley et al. (2016), (7) Schady et al. (2012), (8) Hjorth et al. (2012), (9) Blanchard et al. (2016), (10) Zafar et al. (2011), (11) McGuire et al. (2016), (12) Zafar et al. (2010), (13) Covino et al. (2013), (14) Perley et al. (2009), (15) Basa et al. (2012), (16) Laskar et al. (2011), (17) Perley et al. (2013), (18) Krühler et al. (2011), (19) D'Avanzo et al. (2010), (20) Greiner et al. (2015), (21) Thöne et al. (2013), (22) Sparre et al. (2014), (23) D'Elia et al. (2014), (24) Friis et al. (2015), (25) Cannizzo et al. (2013).

$z = 3$, which suggests that these are not interloping DLA or Lyman-limit systems.

Out of 59 GRB-DLAs, 45 have GRB host galaxy photometric detections in at least one band or we are able to measure photometric limits in the rest-frame ultraviolet (UV), which directly traces star formation. We do not use any photometry that is below the Lyman-limit in the host galaxy rest-frame and our spectral energy distribution (SED) modeling

Table 2
GRB Sub-DLAs

GRB sub-DLA	Redshift[a]	log $N_{\rm H\,I}$ ($\rm cm^{-2}$)	log $Z/Z_\odot$	A_V	SFR[b] ($M_\odot\ \rm yr^{-1}$)	log M_* ($M_\odot$)	log $M_{\rm dust}$ ($M_\odot$)	References
021004	2.3289	19.00 ± 0.20	⋯	0.038	$7.19^{+0.17}_{-1.21}$	$9.29^{+0.06}_{-0.32}$	$9.29^{+0.06}_{-0.32}$	(1), (2)
050908	3.344	19.40 ± 0.20	⋯	<0.550[c]	$3.21^{+1.65}_{-1.09}$	⋯	⋯	(3), (4)
060124	2.3	18.50 ± 0.50	⋯	0.170 ± 0.030[c]	$0.46^{+0.10}_{-0.07}$[d]	⋯	⋯	(5), (6)
060526	3.221	19.90 ± 0.15	⋯	0.700 ± 0.180[c]	$1.63^{+0.91}_{-0.43}$[d]	⋯	⋯	(6), (7)
060605	3.773	18.90 ± 0.40	⋯	⋯	$0.40^{+0.06}_{-0.05}$	⋯	⋯	(5)
060607A	3.075	16.95 ± 0.03	⋯	0.080 ± 0.040[c]	<0.29	⋯	⋯	(3), (8)
080310	2.427	18.70 ± 0.10	⋯	0.100 ± 0.020[c]	$1.82^{+1.14}_{-0.51}$[d]	⋯	⋯	(4), (7)
080810	3.35	17.50 ± 0.15	⋯	⋯	$27.33^{+15.99}_{-10.09}$	⋯	⋯	(9)
080913	6.69	<19.84	⋯	0.120 ± 0.030[c]	<1.51	⋯	⋯	(10), (11)
090323	3.5778	>19.90	⋯	⋯	$9.72^{+1.75}_{-1.49}$	⋯	⋯	(12)
090426	2.609	19.10 ± 0.15	⋯	0.088	$3.03^{+0.00}_{-0.00}$	$8.48^{+0.00}_{-0.00}$	$8.48^{+0.00}_{-0.00}$	(13)
130606A	5.9134	19.93 ± 0.20	⋯	⋯	$1.63^{+0.37}_{-0.25}$[d]	⋯	⋯	(14)

Notes.
[a] Significant digits of redshift reflect accuracy of measurement.
[b] Dust-corrected (except those without A_V measurements).
[c] Host extinction from GRB afterglow measurements.
[d] Calculates SFR from MAGPHYS SED scaling of photometric detection. (1) Fynbo et al. (2005), (2) de Ugarte Postigo et al. (2005), (3) Hjorth et al. (2012), (4) Perley et al. (2009), (5) Blanchard et al. (2016), (6) Kann et al. (2010), (7) Perley et al. (2016), (8) Schady et al. (2012), (9) Greiner et al. (2015), (10) Basa et al. (2012), (11) Zafar et al. (2011), (12) McBreen et al. (2010), (13) Thöne et al. (2011), (14) McGuire et al. (2016).

accounts for IGM absorption (described in detail in Section 3.1.1) for the three GRB-DLA and one GRB sub-DLA host galaxies that have photometric detections in the rest-frame Lyα forest. Throughout our paper, we refer to these 45 GRB-DLAs as our sample (Table 1). Our sample has a median $z = 3.2$ and log $N_{\rm H\,I} = 21.6$.

For completeness, we also include 12 sub-DLAs in Table 2.

2.2. LMI Data Reduction

We use LMI to add five upper limits and one detection of DLA galaxy counterparts. The LMI data were detrended with a custom IRAF[9] pipeline. Individual frames were astrometrically aligned with `Scamp` (Bertin 2006) and coadded using `SWarp` (Bertin et al. 2002). We performed aperture photometry on the resulting coadded images using `Sextractor` (Bertin & Arnouts 1996) with a static 5 pixel (1.″2) radius aperture, which is typical of the average seeing. The resulting magnitudes were calibrated against the SDSS; (Aihara et al. 2011) fields.

2.3. Comparison to Other Samples

We compare the observer frame R-band and redshift distribution of our sample with The Optically Unbiased Gamma-ray burst Host (TOUGH) survey (Hjorth et al. 2012, see Figure 1). Our DLA sample covers the $z \sim 2$–6.3 redshift range and a similar R-band luminosity distribution (which is usually a good proxy for the host rest-frame UV luminosity) as TOUGH. In the cases where R-band is not available but we have r' or F606W observations, we convert to R-band assuming a flat SED between these three filters. Additionally, 11 GRB-DLAs do not have R-band, r'-band, or F606W observations (either detections or limits). For these GRB-DLAs, we scale the modeled SEDs (see Section 3.1.1) from our small sample of eight GRB-DLA counterparts with extensive photometric coverage to the observed magnitude and present the median scaled R-band value of those eight SEDs in Figure 1. Note that if the standard deviation of the R-band value from those eight SEDs was larger than the median we report it as an upper limit. Also, at $z \gtrsim 4$, the R-band traces flux emerging at or below the Lyα line (1216 Å rest-frame); therefore, these values are more uncertain since they are subject to additional absorption.

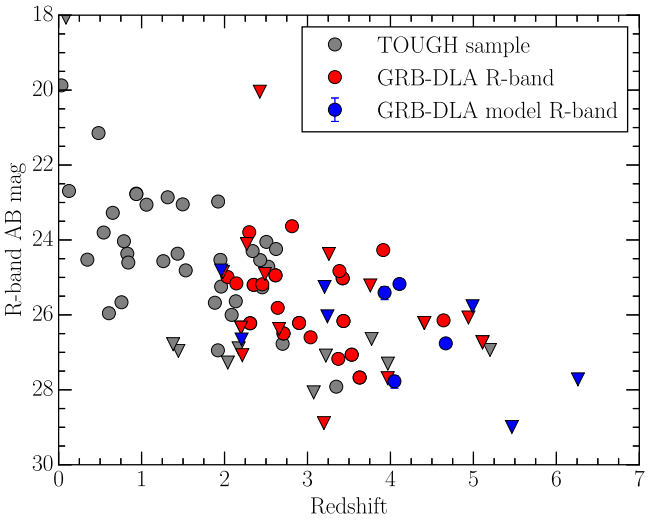

Figure 1. Distribution of R-band observations of GRB host galaxies with redshift; all data have been corrected for Galactic extinction. Downward triangles are upper limits and circles are detections. Red points are from R, r', F606W observations, using a flat SED to calculate R-band AB magnitude. Blue points are from using scaled SEDs from MAGPHYS (Section 3.1.1) to determine R-band AB magnitudes (see the text for details).

After we remove objects from our sample that are in the TOUGH survey, we run a two-sample Kolmogorov–Smirnov test on the redshift distribution (see Figure 2) over the overlapping redshift range of $z \sim 2$–5. The p-value of 0.78 is

[9] IRAF is distributed by the National Optical Astronomy Observatories, which are operated by the Association of Universities for Research in Astronomy, Inc., under cooperative agreement with the National Science Foundation.

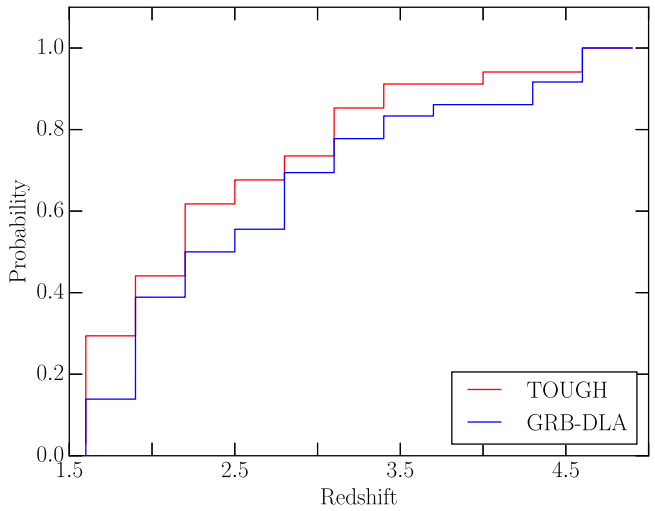

Figure 2. Cumulative redshift distribution of our GRB-DLAs compared with that of the TOUGH sample. Two-sample Kolmogorov–Smirnov tests show that our sample is consistent with being drawn from the same redshift distribution as TOUGH.

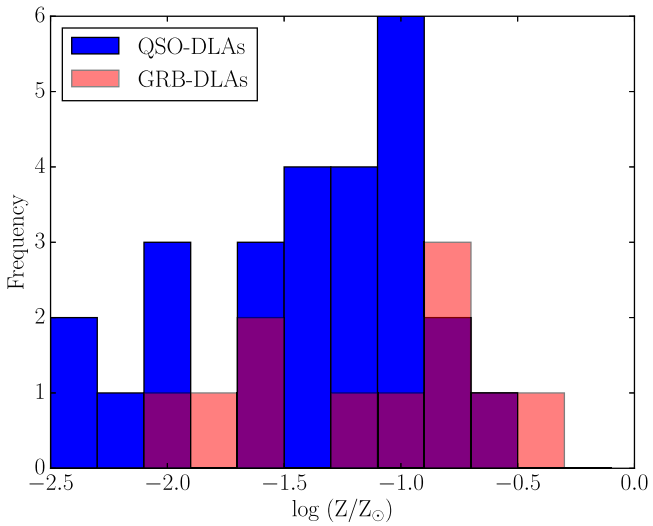

Figure 3. Metallicity distribution of our sample compared with the Fumagalli et al. (2014) double-DLA sample. The majority of our absorption-line metallicity measurements are lower limits which we do not include in this histogram.

consistent with our GRB-DLA counterpart sample and the TOUGH survey being drawn from the same GRB host population. To the extent that TOUGH is a representative sample of the overall GRB host population, this means that the GRB-DLAs hosts are also representative of the overall GRB host population.

We also compare our sample throughout this paper to the Fumagalli et al. (2010) sample of QSO-DLAs studied with the double-DLA technique, which has no selection bias toward large impact parameters. Our sample (which covers the $N_{\rm H\,I} = 10^{20.4-22.7}\,{\rm cm}^{-2}$ range) represents an extension of the work by Fumagalli et al. (2015), which probes mainly lower column densities ($N_{\rm H\,I} = 10^{20.2-21.2}\,{\rm cm}^{-2}$), providing further insights on the nature of the overall DLA counterpart population (see Prochaska et al. 2007). We perform a Kolmogorov–Smirnov test on the column density distribution over the overlapping column density range of $N_{\rm H\,I} = 10^{20.2-21.2}\,{\rm cm}^{-2}$ and the p-value of 0.74 is consistent with our GRB-DLA counterpart sample and the QSO-DLA sample being drawn from the same DLA population for that range of column densities. However, we caution that these samples may not be from the same population for reasons discussed throughout the paper and because this p-value suffers from problems associated with small number statistics.

Unfortunately, it is difficult to compare our GRB-DLA metallicities with other samples because the majority of our metallicities are lower limits. Instead, we only plot a histogram of our 11 GRB-DLA metallicity detections compared to the double-DLA sample (Figure 3); our sample covers a similar spread in metallicity as the double-DLA sample with the exception of a handful of metal-rich systems above $\log(Z/Z_\odot) > -1$. For a more detailed analysis of our sample's metallicity distribution and a direct comparison with the largest compilation of QSO-DLAs to date, we direct the reader to the extensive published work by Cucchiara et al. (2015) and Rafelski et al. (2012, 2014).

3. STAR FORMATION

Star formation is correlated with the neutral gas content in a galaxy, but it is not completely clear which phase has a stronger causal connection with star formation: atomic, molecular, or total hydrogen (Schmidt 1959; Kennicutt 1998; Krumholz et al. 2009; Rafelski et al. 2011, 2016; Elmegreen 2015). Here we use atomic neutral hydrogen column densities measured from the damped Lyα absorption feature and assume that the molecular hydrogen has a negligible contribution. This is supported by the small ($\sim$1%) molecular hydrogen detection rate in a blind and uniformly selected DLA survey (Jorgenson et al. 2013, 2014) and by targeted surveys (Noterdaeme et al. 2008).

Additionally, it is rare to detect molecular absorption features in GRB afterglow spectra (supported by the few H_2 measurement along few GRB lines of sights, e.g., Prochaska et al. 2009; Krühler et al. 2013; D'Elia et al. 2014; Stanway et al. 2015) due to the unavailability of the required high-resolution instruments and blue spectral coverage.

We caution that the GRB afterglow line-of-sight is probing a much smaller area (approximately parsec scale) of the much larger galaxy (approximately kiloparsec scale); however, if GRBs occur in star-forming regions, we expect them to encounter molecular hydrogen whereas the QSO may be ouside of the star-forming region.

We calculate SFRs from rest-frame UV luminosities (see Section 3.1) and investigate if there is any correlation with redshift or the ISM metallicities (as determined by the absorption features). We then calculate SFR surface densities and H I surface densities to explore star formation efficiencies (Section 3.2), and finally we examine possible redshift and absorption metallicity trends in comparison with the Kennicutt–Schmidt relation at both local, $z = 0$, and at higher redshifts (from cosmological simulations).

3.1. Star Formation Rates

We calculate SFRs using three methods. The first and preferred method is SED modeling using MAGPHYS described in Section 3.1.1. We limit the use of SED modeling to GRB-DLA counterparts that have photometric detections in at least three separate bands which is the minimum for MAGPHYS to converge to a reasonable SED fit (though with

large parameter error bars in cases with few photometric points). The second method is using single-band detections corresponding to rest-frame UV bandpass to calculate rest-frame UV SFR (see Section 3.1.2). For consistency, we compare SFRs based on the first two methods: SFR values from these two methods reasonably agree with each other usually within a factor of two, but in rare cases may vary by a factor of five, which is most likely due to different accounting of dust extinction. Generally, the single-band SFRs are in agreement or are slightly lower than those derived from SED modeling with MAGPHYS.

If we are unable to use either of the first two methods and we have at least one detection in another filter, we scale the SEDs from the DLA counterparts that were fit with the first method to match the detected host galaxy flux. We then use the scaled SEDs to estimate the rest-frame UV flux and use the median and standard deviation of the scaled SEDs to calculate the rest-frame UV SFR. Finally, if there are no detections in any band but there are upper limits in the rest-frame UV band, we calculate SFR upper limits using the second method.

Photometric measurement were made using the aperture photometry technique, using the *HST* point-spread function (PSF) for GRB-DLA counterparts with *HST* data and the DCT 1.″2 PSF for the ground-based data (corresponding to ∼2 and ∼17 kpc diameter apertures respectively). The large difference in apertures comes from the fact that *HST* is able to resolve the host galaxy. We assume that the light from unresolved sources is solely from the host galaxy and background sky.

All SFRs are calculated from dust-corrected observations unless otherwise stated. The host extinction, A_V, is taken either from SED models or from GRB afterglow measurements using a Small Magellanic Cloud (SMC)-like extinction law which has been shown to best depict the GRB explosion environment (e.g., Schady et al. 2012).

We assume the host extinction is the same as the GRB line-of-sight extinction, which Perley et al. (2013) has shown is fairly consistent within a factor of two to three. If the host extinction is an upper limit, we use that value in all dust-corrected calculations and report SFR upper limits. In Table 1, we report these GRB-DLAs with SFR error estimates but treat these as SFRs upper limits in all plots using dust-corrected SFRs. Our host extinction is, in general, higher than the $A_V \lesssim 0.1$ reported for DLAs in the SDSS survey for our sample's column densities (Murphy & Bernet 2016). This may likely be because GRB-DLAs are found at a smaller impact parameter of $\lesssim$5 kpc (Blanchard et al. 2016) than the general DLA population of 1–25 kpc (Fumagalli et al. 2015) or more simply because our DLA sample traces, in general, metal-rich, and likely dust rich, systems (for example, see the correlation between $E(B-V)$ and metal line equivalent widths in Murphy & Bernet 2016).

3.1.1. SED Fitting Star Formation Rate

We use MAGPHYS with the `HIGHZ` extension (da Cunha et al. 2008, 2015), to model the host galaxy SEDs from photometry. MAGPHYS models templates to the data and returns an SED with fitted parameters which include SFR, stellar mass (M_*), dust mass ($M_{\rm dust}$), and A_V. This particular package is well suited for $z > 1$ galaxies and takes into account bursty star formation which is appropriate for GRB host galaxies as suggested by Hunt et al. (2014). MAGPHYS uses a continuous model of star formation with superimposed random bursts that happen at equal probability at all times up to the age of the galaxy. The probability is set such that 50% of the galaxies within the library have had a burst of star formation within the past 2 Gyr with bursts lasting $\sim 10^7$–10^8 years. MAGPHYS also accounts for IGM absorption and uses a Gaussian distribution centered around the mean IGM effective absorption from Madau (1995) for each model template.

We only select objects that have at least three photometric detections in order to break some parameter degeneracy and then include, if available, upper limits. We have nine GRB-DLAs that fit this criterion; however, GRB 080607 returns an unconstrained SFR and M_*. This particular host galaxy has an extremely high host extinction and H I column density that is atypical of the majority of galaxies (Prochaska et al. 2009; Chen et al. 2010; Perley et al. 2011; Wang et al. 2012).

3.1.2. Single-band UV SFR

We use the relations for UV luminosities from Savaglio et al. (2009) to determine SFR from a single photometric band:

$$\mathrm{SFR}_{1500} = 1.62 \times 10^{-40} \frac{L_{1500,\mathrm{corr}}}{\mathrm{erg\ s^{-1}\ \AA^{-1}}}\ M_\odot\ \mathrm{yr^{-1}} \quad (1)$$

$$\mathrm{SFR}_{2800} = 4.33 \times 10^{-40} \frac{L_{2800,\mathrm{corr}}}{\mathrm{erg\ s^{-1}\ \AA^{-1}}}\ M_\odot\ \mathrm{yr^{-1}} \quad (2)$$

$$\mathrm{SFR}_{3600} = 5.47 \times 10^{-40} \frac{L_{3600,\mathrm{corr}}}{\mathrm{erg\ s^{-1}\ \AA^{-1}}}\ M_\odot\ \mathrm{yr^{-1}}. \quad (3)$$

Equations (1)–(3) were derived from samples with simultaneous Hα and UV detections suitable for GRB host galaxies and are for dust-corrected rest-frame UV luminosities. In Figure 4, we present only dust-uncorrected rest-frame UV luminosities to directly compare with Fumagalli et al. (2015), but in all other figures and tables we present dust-corrected rest-frame UV SFRs. We note that other objects that we compare with in this paper use Hα to SFR conversions from Kennicutt (1998; e.g., Fumagalli et al. 2015 and Rafelski et al. 2016): direct comparison to Savaglio et al. (2009) can result in a difference of a factor of $\lesssim$2 in SFRs (which includes factors for different initial mass functions).

To determine rest-frame UV SFR, we consider observations redward of the rest-frame Lyα line and from filters that have rest-frame effective wavelengths within 250 Å of 1500 Å, 2800 Å, or 3600 Å when we use these relations. We have 12 GRB-DLAs with rest-frame UV detections (four of which have A_V upper limits so we list the SFRs as upper limits) and 12 GRB-DLAs with rest-frame UV limits.

Additionally, we have another 12 GRB-DLAs that have detections redder than the rest-frame UV (one of which has an A_V upper limit so we list the SFR as an upper limit). We use the scaled SEDs from the eight GRB-DLAs fit with MAGPHYS (we do not include GRB 080607 in this fit for reasons described in Section 3.1.1) and calculate the SFR using Equations (1)–(3) for the closest wavelength to our rest-frame observed effective wavelength. We report the median and standard deviation SFR of these eight scaled SEDs in Table 1. We also find that our SFR measurements are in good agreement with literature values (e.g., SHOALS sample; Perley et al. 2013).

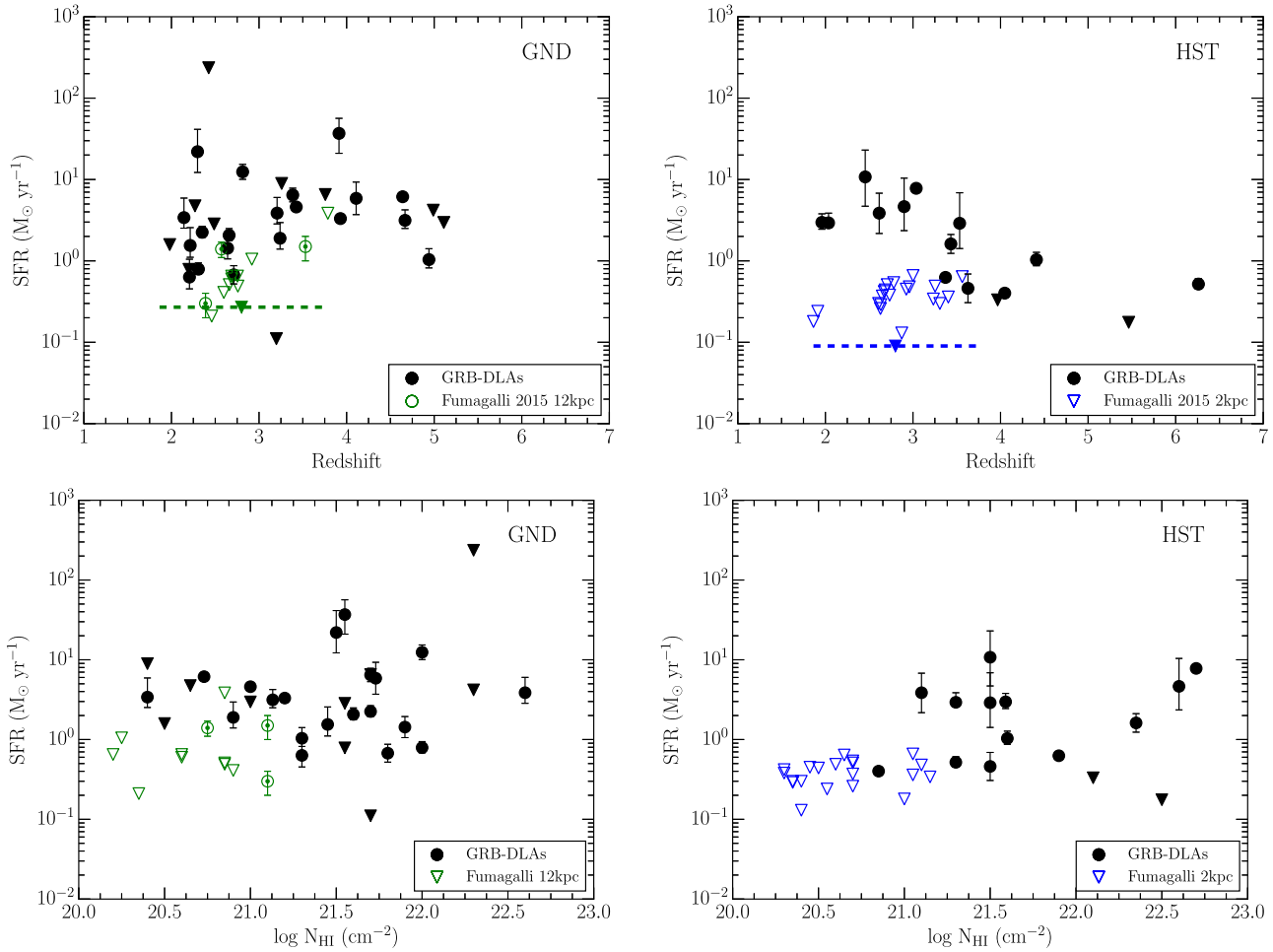

Figure 4. Comparing SFRs in our sample (black points) with Fumagalli et al. (2015) double-DLA SFRs (green/blue unfilled points) for both ground-based and *HST* data. Both data sets are uncorrected for dust for direct comparison. Triangles represent upper limits. Our sample uses the DCT 1.″2 PSF (∼17 kpc diameter) apertures for ground-based data and the *HST* PSF (∼2 kpc diameter) apertures for *HST* data. (Top left) Ground-based SFRs vs. redshift. There are three double-DLA detections, but one may be contaminated by the QSO (see Fumagalli et al. 2015 for details). The dashed green line is a deep limit from a composite image. (Top right) *HST* SFRs vs. redshift. The dashed blue line is a deep limit from a composite image. (Bottom left) Ground-based SFRs vs. H I column density. (Bottom right) *HST* SFRs vs. H I column density.

3.1.3. DLA Host SFRs

In Figure 4, we compare the dust-uncorrected SFRs with the dust-uncorrected SFR detections and limits derived by Fumagalli et al. (2015). Similar to this study, we also take full advantage of our large data set and probe in situ DLA counterpart SFRs within compact (∼2 kpc using *HST* data) and more extended regions (∼17 kpc using our ground-based observations). The majority of our sample has generally higher SFRs than the double-DLA limits; however, in some cases, we obtain SFRs similar to the double-DLA limits both from ground-based and *HST* observations (downward triangles). This result displays the effectiveness of targeting GRB-DLA counterparts: not only is our DLA detection rate higher than Fumagalli et al. (2015), but our DLAs (when we combine ground and *HST* data) span a larger range of both redshift and column densities and trace intrinsic SFR over four orders of magnitude (10^{-1}–$10^2\,M_\odot$ yr^{-1}).

Nevertheless, some DLA counterparts identified along QSOs have measured SFRs with 1–30 $M_\odot$ yr^{-1} (see Fumagalli et al. 2015 and references within). It may be that it is more difficult to detect these high SFR DLAs along QSOs using an unbiased impact parameter survey as we mentioned in Section 1 or they may be from an entirely different counterpart population.

We caution that SFRs of DLAs within GRB hosts may be skewed toward higher values than the general DLA population because our sample is taken from long-duration GRBs which are known to be associated with the evolution of massive stars (see Woosley & Bloom 2006 for a review) and are therefore associated with galaxies that have higher specific SFRs (Japelj et al. 2016).

Recent work by Perley et al. (2016) has shown that the $z \gtrsim 2$ GRB host population seems to be consistent with the general cosmic star formation rate, strengthening the idea that our DLA sample may be an important complement to our current understanding of the nature of DLAs.

Also, DLA counterpart SFRs have been predicted to be higher for higher column densities and higher metallicities (Krumholz et al. 2009; Gnedin & Kravtsov 2010; Rafelski et al. 2011, 2016; Noterdaeme et al. 2014; Rahmati & Schaye 2014). Our SFRs appear to be independent of column density in Figure 4: the five detections (including both ground and *HST* data) with $N_{\rm H\,I} \leqslant 10^{21}$ cm^{-2} have similar SFRs of those with high H I column densities and Rahmati & Schaye (2014) simulations show that only 5% of galaxies with

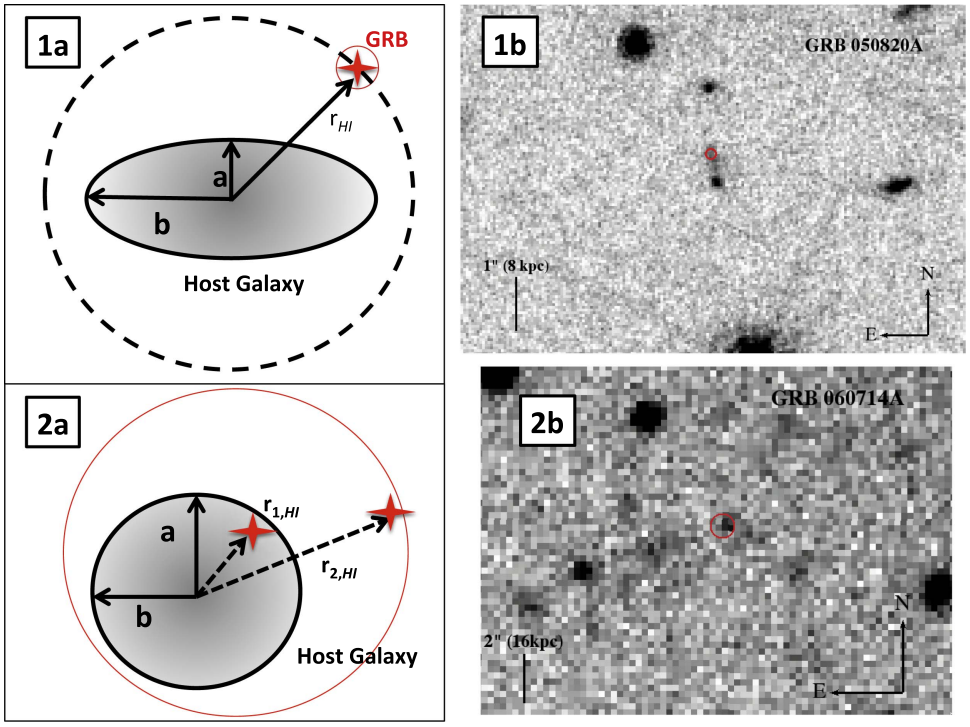

Figure 5. (Top left, (1a)) Ideal case where the GRB, and therefore the H I gas, is extremely well localized (red circle is localization error) and can be identified relative to the host galaxy. (Top right, (1b)) An observed case, GRB 050820A, close to the top-left idealized configuration. The GRB-DLA is localized to sub-arcsec precision (red circle) from rapid follow-up of the afterglow with *HST* and the DLA galaxy has been resolved using *HST*. (Bottom left, (2a)) Realistic case where the GRB, and therefore the H I gas, has a large error circle (red circle) that can place the GRB within the host galaxy or on the outskirts. (Bottom right, (2b)) An observed example, GRB 060714A, close to the bottom-left realistic configuration. The GRB is localized to $\lesssim 1''$ (red circle) and, although observed with Keck, the host galaxy is unresolved.

$N_{\rm H\,I} = 10^{20-21}\,{\rm cm}^{-2}$ have SFRs $>10\,M_{\odot}\,{\rm yr}^{-1}$. Again, we caution that SFR is a global measurement of the host counterpart, whereas H I column density is measured along the line-of-sight of the GRB afterglow and there may be some scatter in the line-of-sight measurement compared to the average DLA H I column density. Since the majority of our metallicity measurements are lower limits, it is difficult to determine if metallicity plays an important role, if any at all, as presented in some cosmological simulations (Rahmati et al. 2016).

We compare our distribution of SFRs within $z = 2$–4 and $N_{\rm H\,I} = 10^{21.5-22}\,{\rm cm}^{-2}$ to simulation results from Rahmati & Schaye (2014) at $z = 3$ with the same $N_{\rm H\,I}$ range. Our sample has a total of 15 objects that meet these criteria and 33% ± 8% of them have SFRs $<1\,M_{\odot}\,{\rm yr}^{-1}$, where we assume the error is primarily poissonian. This number is slightly lower than the predicted 45% by Rahmati & Schaye (2014). While the number of GRB-DLAs in this comparison is still small, future and more complete GRB-DLAs surveys (like the SHOALS survey) will provide more accurate tests for cosmological simulations and the conversion of neutral gas into stars (e.g., stellar mass).

It is also evident from our results that the DLA counterpart SFRs appear to be independent of redshift and our detections are all above the double-DLA upper limits for both the ground-based and the *HST* observed GRB-DLAs, though the higher SFRs measured in the ground data may be affected by the unresolved part of the GRB hosts (especially at high-z). In fact, as pointed out by Fumagalli et al. (2015), resolving the exact location of the emission of the DLA counterparts plays a critical role in our understanding of the DLA properties (see Figure 5), and only more *HST* data, in combination with more accurate GRB afterglow localization will enable precise DLAs in situ SFR measurements. We note, for our current sample, that the probability of chance association with *HST* is typically $\lesssim$0.05, so it is very unlikely that these are interloping galaxies (Blanchard et al. 2016), but are indeed regions of star formation within the GRB host (Figure 5, panels (1a) and (1b)).

3.2. Kennicutt–Schmidt Relation

The Kennicutt–Schmidt relation (KS-relation) connects the available neutral hydrogen gas surface density to form stars ($\Sigma_{\rm H\,I}$) to the actual measured SFR surface density ($\Sigma_{\rm SFR}$). The KS-relation has been extensively studied in the local universe (Bigiel et al. 2008, 2010; Bolatto et al. 2011; Elmegreen 2015). As we mentioned previously, we only consider the atomic hydrogen gas content since the molecular hydrogen gas has a negligible contribution at these H I column densities. This scenario may change with redshift, metallicity, or the actual regions in which the SFR is measured—core versus outskirts of galaxies (e.g., Glover & Clark 2012; Krumholz 2012, 2013; Rafelski et al. 2016).

3.2.1. Surface Density Estimates

In order to measure $\Sigma_{\rm H\,I}$, which is estimated *along the line-of-sight of the GRB*, we assume that the neutral gas is equally distributed across the entire PSF used for determining our SFR density. Figure 5 shows the idealized case (panel (1a)), where the GRB is well localized and the host galaxy is resolved. We include an observed example of this idealized case (panel (1b)) for the DLA galaxy identified in the *HST* image of GRB 050820A (cigar shaped with bright nucleus to the south;

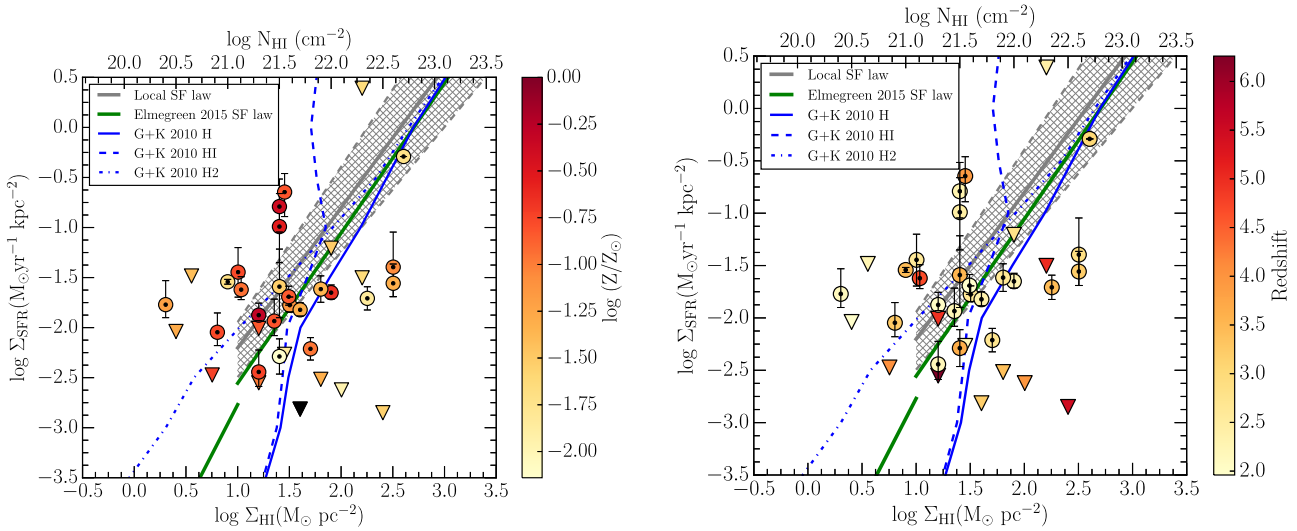

Figure 6. Dust-corrected SFR surface densities vs. H I gas surface densities of our GRB-DLA counterpart sample. We do not include GRB-DLAs that do not have host dust extinction measurements. Upper limits are shown as triangles as are GRB-DLAs with host extinction upper limits. We overplot the local Kennicutt–Schmidt relation with errors (gray and gray hash; Schmidt 1959; Kennicutt 1998), the local SF law from Elmegreen (2015; green), and $z \sim 3$ Gnedin & Kravtsov (2010) simulations for total hydogren, atomic, and molecular gas (blue solid, dashed, and dotted respectively). The *total* neutral gas from Gnedin & Kravtsov (2010) SF laws should be shifted to the right since we are plotting against the *atomic* hydrogen gas content. Additionally, the *molecular* hydrogen gas should be shifted to the left since we expect there to be more *atomic* hydrogen gas than *molecular* hydrogen gas. (Left) SFR surface densities vs. H I gas surface density color coded with metallicity; black points have no metallicity measurements from absorption lines. (Right) SFR surface densities vs. H I gas surface density color coded with redshift.

see Blanchard et al. 2016 for compilation of GRB host galaxy morphologies): the GRB location is identified with sub-arcsec precision due to rapid follow-up of the afterglow with *HST* (red circle in (1a) and (1b) panels), and is in the outskirt of the host galaxy (at radius $r_{\rm H\,I}$). Moreover, the $N_{\rm H\,I}$ column is measured through the same environment (which may vary at smaller impact parameters).

However, in general, due to the high-redshift nature and the quality of our data, we encounter a less ideal scenario, as shown in Figure 5 panels (2a) and (2b). The uncertainty in the GRB localization, despite being often $\lesssim 1''$ ($1''$ is ~6–9 kpc for $z = 2$–6), combined with the unresolved host morphology do not allow us to accurately measure $\Sigma_{\rm H\,I}$ and $\Sigma_{\rm SFR}$. In particular, as evident in panel (2a), the uncertainty in the GRB localization (red circle) makes it difficult to determine the actual neutral hydrogen line-of-sight ($r_{1,\rm H\,I}$ and $r_{2,\rm H\,I}$ are equally viable, but clearly probe two very different environments).

In order to be consistent with the local observed KS-relation and the higher-z theoretical models, we calculate $\Sigma_{\rm SFR}$ using our dust-corrected SFR calculated in Section 3.1 and the area covered by the unresolved ground-based aperture ($1\farcs2$ radius aperture) around the GRB location, which correspond to a circular area of ~17 kpc diameter for $z = 2$–6 (astropy's FlatLambdaCDM; Astropy Collaboration et al. 2013), for all the objects in our sample. While this area decreases the $\Sigma_{\rm SFR}$ for our resolved *HST* objects by a factor of ~70, this allows us to be consistent when we compare both our resolved and unresolved observations to other samples and models.

Furthermore, in this context, we derive the atomic gas (H I) surface density, $\Sigma_{\rm H\,I}$, directly from the DLA line-of-sight neutral hydrogen column density as shown by Lanzetta et al. (2002) and Hopkins et al. (2005) even though $\Sigma_{\rm H\,I}$ and $\Sigma_{\rm SFR}$ are measured over different scales, the KS-relation is, on average, still valid (see also, e.g., Zwaan & Prochaska 2006; Wolfe & Chen 2006; Rafelski et al. 2011, for the limitations of such approximation). This is clearly an oversimplification, but it is consistent with the analyses from other SF laws and cosmological simulations. Note that we do not include GRB-DLAs that have no A_V measurements as the dust-corrected SFR measurements are usually lower limits.

3.2.2. Comparision with Star Formation Laws and Simulations

With these caveats in mind, and in order to be consistent with previous works, we overplot the local Kennicutt–Schmidt relation of $\Sigma_{\rm SFR} = K\left(\frac{\Sigma_{\rm H\,I}}{\Sigma_0}\right)^{\beta}$ with $K = (2.5 \pm 0.7) \times 10^{-4}\, M_\odot\ {\rm yr}^{-1}\,{\rm kpc}^{-2}$, $\beta = 1.40 \pm 0.15$, and $\Sigma_0 = 1\, M_\odot\ {\rm pc}^{-2}$ (Kennicutt 1998) in Figure 6 along with a dynamical star formation law for spiral and irregular galaxies (Elmegreen 2015) and a star formation law at $z \sim 3$ from cosmological simulations (Gnedin & Kravtsov 2010). Note that the Gnedin & Kravtsov (2010) SFR surface density is shown for the total neutral hydrogen gas (dash blue line), only molecular hydrogen gas (dotted–dashed blue line), and only atomic hydrogen gas (solid blue line). We also, in the two panels, color code our points based on GRB afterglow absorption-line metallicity (left) and redshift (right). The interpretation of this plot is clearly non-trivial: a large fraction (~50%) of our detected DLA counterpart falls in the predicted local K–S relation (shaded area), while some very low metallicity systems are below. Moreover, the presence of our upper limits seem to indicate a very low $\Sigma_{\rm SFR}$ for the amount of measured $\Sigma_{\rm H\,I}$. These discrepancies can be due to different factors: GRB afterglow measured metallicities may be lower than the average DLA host metallicity or the distribution of neutral hydrogen may be poorly approximated (Lanzetta et al. 2002; Hopkins et al. 2005). Finally, while we emphasize here that most of our metallicity estimates are lower limits, the $z \sim 3$ theoretical predictions seem to better predict some of the low metallicity and high metallicity systems.

In Figure 7, we overlay our DLA counterparts onto results from Krumholz (2014) showing the star formation efficiencies in LBG outskirts (Rafelski et al. 2011, 2016), previous DLA upper limits (Wolfe & Chen 2006), double-DLA composite

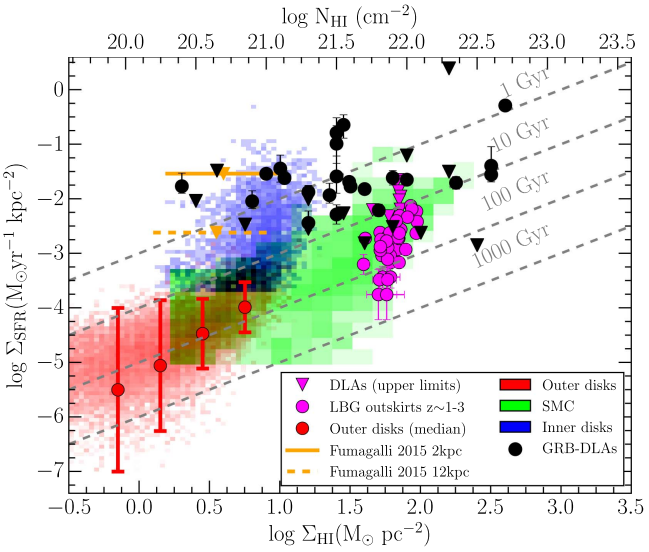

Figure 7. Dust-corrected SFR surface densities vs. H I gas surface densities from our GRB-DLAs (black) on top of the compilation of observed SFR surface density vs. gas surface density from Krumholz (2014). The purple points are Lyman-break galaxy outskirts at $z \sim 1$–3 (uncorrected for dust) from Rafelski et al. (2011, 2016), the purple triangles are DLA limits from Wolfe & Chen (2006), the orange triangles with error bars are composite image limits from dust-uncorrected double-DLAs from Fumagalli et al. (2015). The red pixels are from lines-of-sight through the outer disks of local spiral and dwarf galaxies (Bigiel et al. 2010). The red circles are the median and $1-\sigma$ scatter. The blue pixels are from the inner parts of local galaxies (Bigiel et al. 2008). The green pixels are from the SMC (Bolatto et al. 2011). Note the SMC, LBG outskirts, and DLA limits are actually plotted for the SFR surface densities vs. the *total* neutral hydrogen gas surface densities, not the *atomic* hydrogen gas surface density. We expect that adjusting these measurements to the H I gas surface densities will move the points to the left. The gray dashed lines mark constant depletion times ($t_{\rm dep} = M_{\rm gas}/{\rm SFR}$).

image limits (Fumagalli et al. 2015), the outer disks of local spiral and dwarf galaxies using 21 cm emission to measure H I (Bigiel et al. 2010), the inner disks of the local using 21 cm emission to measure H I (Bigiel et al. 2008), and the SMC (Bolatto et al. 2011). Rafelski et al. (2011, 2016) report dust-uncorrected $\Sigma_{\rm SFR}$ and use a different SFR conversion (see Section 3.1.2), which may partially explain our higher $\Sigma_{\rm SFR}$ for GRB-DLA hosts (though some discrepancies may still remain). We note that Krumholz (2014) originally plotted the SFR surface density against *total* neutral hydrogen gas surface density not the *atomic* hydrogen gas surface density. We expect that adjusting these measurements to H I gas surface densities will shift the magenta points to the left in the plot.

We also overplot lines of constant depletion times, $t_{\rm dep} = M_{\rm gas}/{\rm SFR}$. Depletion time represents how long it would take to completely use up the neutral gas (in this case, H I) with a constant SFR. Our sample covers a large range of depletion times, some of which are longer than the age of the universe as seen by the galaxy at the DLA redshift. This indicates that some of these systems have not reached equilibrium yet and that we are measuring a phase of lower star formation than in earlier times.

Our GRB-DLA counterparts seem to show no overlap with local outer disk galaxies and seem to have similar depletion times as inner galaxy disks, the SMC, and LBG outskirts (in a few cases). This is consistent with the observational evidence that GRB hosts are compact, SMC-type, star-forming galaxies (see also Noterdaeme et al. 2012a). However, we would caution the reader that GRB-DLAs may sample higher SFRs than QSO-DLAs because GRBs are associated with massive stars that are typically in galaxies with higher specific SFRs. From the DLA counterpart perspective this shows that our sample traces DLAs with shorter depletion times than other DLAs or LBG outskirts (magenta dots; note that these points are dust-uncorrected SFRs), and that its higher metallicity, typically 1%–20% the solar value, can be the cause of this offset (see Krumholz 2014). For the same reason, most of the magenta points in Figure 7 have much longer depletion times at fixed gas surface density than most local spirals.

4. ENRICHMENT TIME

Star formation is the only process responsible for metal production. Supernova feedback and stellar winds, on the other hand, contribute to the dispersion of metals toward the outer regions or even outside the galaxy's potential well. The enrichment time is used to determine if the current SFR can solely account for the current measured metallicity and the metal build up of these systems. We assume a very simple scenario where the SFR is constant and the metal mass is calculated from the absorption-line metallicity measured from GRB afterglow spectra ("closed box" model).

We calculate the mass in metals:

$$M_{z,\rm obs} = 10^{[\rm X/H]} Z_\odot m_p N_{\rm H\,I} \pi r^2 \quad (4)$$

where [X/H] is the metallicity measured from absorption listed in Table 1, assuming $Z_\odot = 0.0181$ (Asplund et al. 2009) and r is the radius that we take to be $1\farcs2$ across all redshifts. We then assume that the observed mass in metals is solely due to star formation and we can calculate the enrichment time, Δt_z, from

$$M_{z,\rm SFR} = y_z \dot{\psi} \Delta t_z \quad (5)$$

where we assume a metal yield of $y_z = 1/42$ (Madau et al. 1996) and use SFRs ($\dot{\psi}$) from Table 1. Note that Equation (4) may overestimate the mass of metals particularly because the metals could be not fully mixed and absorption features typically arise in highly enriched gas. This may lead to inflated enrichment times.

We plot enrichment time against metallicity (Figure 8) and overplot the time since $z = 10$ to $z = 2$ and $z = 6$ (where most of our DLAs are found). Some of our DLA counterparts have enrichment times shorter than the age of their host galaxy. This indicates that these galaxies have an underabundance of metals if the metals were formed from a constant SFR. Therefore, it suggests that these systems could have gone through episodic star formation or that feedback expelled metals from the galaxy (stellar or supernova feedback; Davé & Oppenheimer 2007; Rahmati et al. 2016). On the other hand, other DLA hosts have enrichment times longer than the age of the galaxy. This means there is an over abundance of metals if the metals were formed from a constant SFR. This may be evidence of either episodic or exponentially declining star formation, poor mixing between the metals within the DLA and the rest of the host galaxy, or another source of metal enrichment such as an influx of metal-enriched gas from galaxy mergers. The former have been also invoked by Hunt et al. (2014), which has shown that a significant amount of the total stellar mass ($\geqslant$10%) of some GRB host galaxies can be created in very short ($\sim$50 Myr) star formation episodes.

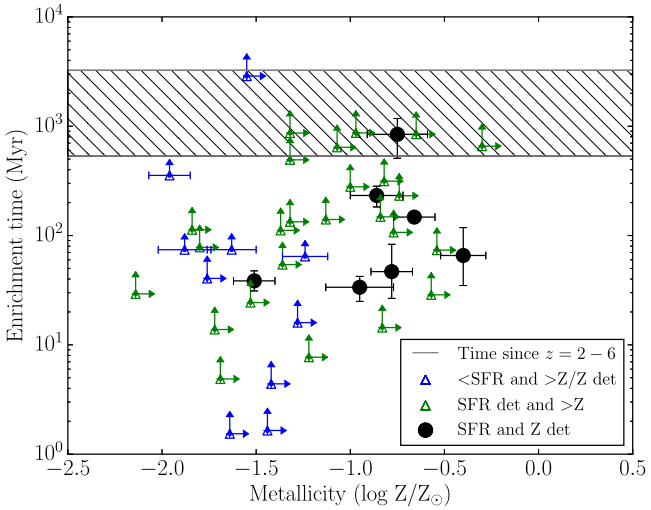

Figure 8. Enrichment time assuming that the galaxy has maintained a constant SFR and that the observed absorption-line metallicity is the same as the galaxy-wide metallicity, which is purely determined by internal star formation activity. We only have lower limits or detections for metallicity and upper limits and detections for SFRs. Limits are plotted with triangles and the colors represent detected SFRs (green) or upper limit SFRs (blue). Black circles have measured metallicity and measured SFR. The hatched gray area is the time from $z = 10$ to our DLA redshifts of 2–6.

5. SUMMARY AND CONCLUSIONS

We present a sample of 45 DLA galaxy counterparts from photometric follow-up of the GRB host locations. We use a sample of spectroscopically confirmed GRB-DLAs identified in Cucchiara et al. (2015) and collect all the publically available GRB host galaxy photometry. We supplement these observations with DCT-LMI photometric follow-up. We present 33 DLA galaxy counterpart detections (though 5 only have A_V upper limits) and 12 upper limits. This quadruples the number of detected DLA counterparts known to date (previously 13, all of which are QSO-DLAs). These GRB-DLAs have a wider range of H I column densities than QSO-DLAs because they are likely located at much smaller impact parameters than QSO-DLA host galaxies.

Our rest-frame UV SFRs are usually higher than QSO-DLA in situ identified using the double-DLA technique (Fumagalli et al. 2015) and, while long GRBs come from high SFR areas within their galaxies, we still have upper limits that are consistent with the double-DLA sample as well as other DLA surveys (see Table 2 in Fumagalli et al. 2015). From our sample, the SFR does not seem to be correlated with either redshift or column density, and we cannot determine if SFR correlates with DLA metallicity due to the effect of line saturation and blending in GRB afterglow spectra.

We investigate how our sample relates to the Kennicutt–Schmidt relation by looking at the relationship between star formation surface density and H I column density. Our GRB-DLA galaxy counterpart sample spans both higher and lower efficiency of star formation compared to a variety of star formation laws (local Kennicutt–Schmidt relation; Schmidt 1959; Kennicutt 1998; Elmegreen 2015 SF laws, and Gnedin & Kravtsov 2010 simulations at $z \sim 3$). We also compare our sample to objects in the local universe and find that our sample is not consistent with the star formation efficiencies of local spiral and dwarf galaxies. Instead, we find similar efficiencies to local universe inner disks, SMC, and LBG outskirts, complementing what has been currently observed from QSO-DLA counterparts. We caution the reader that our SFRs represent a measurement performed over the integrated host galaxies light while the H I column densities are measured locally along the line-of-sight of the GRB afterglows and may be subject to observational biases (metal-rich, star-forming environments) compared to the average H I column density of the DLAs.

We also examine the depletion times of our systems. Depletion time is a measure of how long it would take to completely deplete the DLA gas, H I gas in our case, assuming that the current SFR remains constant. Our sample spans a large range of depletion times (1–100 Gyr). Some of the our sample's depletion times are longer than the current age of the universe as seen by the galaxy, which indicates that these systems have not reached equilibrium yet.

Finally, we investigate the enrichment time of our DLA host counterparts. Enrichment time is the measure of how long it would take to form all the current metals assuming they were solely formed from star formation at the current constant SFR. Some DLA counterparts have enrichment times that are much shorter than the age of the galaxy, which indicates that the galaxy underwent episodic star formation. Some DLA counterparts have enrichment times that are longer than the age of the galaxy which indicate an over abundance of metals assuming a constant SFR. This suggests that these galaxies may have had episodic star formation histories, there may be other sources of metal enrichment such as galaxy mergers, or that there is poor metal mixing between the metals in the DLA and the rest of the host galaxy.

The higher detection rate of GRB-DLA host galaxies and their properties (e.g., SFR, metallicity) may indicate that QSO-DLAs are an entirely different population than GRB-DLAs. While an investigation of this issue is beyond the scope of this study, we note that such a difference may be due to an intrinsic bias in the GRB-DLA sample such that they represent actively star-forming regions with special conditions correlated with the likelihood of GRB appearance (e.g., trace different physical regions of galaxy). Additionally, metallicity may affect the GRB environment differently than QSO-DLAs.

GRB-DLAs are unique objects that have good localization and can later be followed up with photometry and spectroscopy. These are key advantages with respect to the identification of DLAs along QSOs. However, it is unclear if these objects are from the same DLA population. Our sample, complementary to the QSO-DLAs, is the largest collection of DLA galaxy counterparts available to date bringing the total number of detected DLA counterparts from 13 to 58. Future deep, multiband, follow-up observations of the remaining GRB-DLAs, in particular, with *HST* and large aperture telescopes, will increase the sample size for comparisons with cosmological simulations. Furthermore, we showed the importance of accurate identification (sub-arcsecond or better) of GRB afterglows in precisely pinpointing the DLA location within their host, especially in lieu of more powerful, parsec scale, simulations. Finally, it will be important to investigate the morphology of DLA hosts, in particular, using GRB host galaxies, which seem to show signs of pair interaction (J. Cooke 2016, in preparation, 2016, private communication) and may open new insights on the nature of DLAs and the in situ star formation.

These results made use of Lowell Observatory's Discovery Channel Telescope. Lowell operates the DCT in partnership with Boston University, Northern Arizona University, the University of Maryland, and the University of Toledo. Partial support of the DCT was provided by Discovery Communications. LMI construction was supported by a grant AST-1005313 from the National Science Foundation.

We gratefully acknowledge M. Krumholtz for sharing his data, which significantly improved the analysis for this paper.

This work was supported by the National Aeronautics and Space Administration (NASA) Headquarters under the NASA Earth and Space Science Fellowship Program (grant NNX12AL70H to V.T.). V.T., J.C., and S.V. were partially supported by NSF/ATI grant 1207785. A.C. is funded by the NASA grant "Multiband Observations of the Most Relativistic Gamma-Ray Bursts," NNX15AP23G. M.R. acknowledges support from the NASA Postdoctoral Program. M.F. acknowledges support by the Science and Technology Facilities Council (grant number ST/L00075X/1).

REFERENCES

Aihara, H., Allende Prieto, C., An, D., et al. 2011, ApJS, 193, 29
Asplund, M., Grevesse, N., Sauval, A. J., & Scott, P. 2009, ARA&A, 47, 481
Astropy Collaboration, Robitaille, T. P., Tollerud, E. J., et al. 2013, A&A, 558, A33
Barnes, L. A., & Haehnelt, M. G. 2009, MNRAS, 397, 511
Basa, S., Cuby, J. G., Savaglio, S., et al. 2012, A&A, 542, A103
Bennett, C. L., Larson, D., Weiland, J. L., & Hinshaw, G. 2014, ApJ, 794, 135
Bertin, E. 2006, in ASP Conf. Ser. 351, Astronomical Data Analysis Software and Systems XV, ed. C. Gabriel et al. (San Francisco, CA: ASP), 112
Bertin, E., & Arnouts, S. 1996, A&AS, 117, 393
Bertin, E., Mellier, Y., Radovich, M., et al. 2002, in ASP Conf. Ser. 281, Astronomical Data Analysis Software and Systems XI, ed. D. A. Bohlender, D. Durand, & T. H. Handley (San Francisco, CA: ASP), 228
Bigiel, F., Leroy, A., Walter, F., et al. 2008, AJ, 136, 2846
Bigiel, F., Leroy, A., Walter, F., et al. 2010, AJ, 140, 1194
Bird, S., Vogelsberger, M., Haehnelt, M., et al. 2014, MNRAS, 445, 2313
Blanchard, P. K., Berger, E., & Fong, W.-f. 2016, ApJ, 817, 144
Blanton, M. R., & Roweis, S. 2007, AJ, 133, 734
Bolatto, A. D., Leroy, A. K., Jameson, K., et al. 2011, ApJ, 741, 12
Bouché, N., Murphy, M. T., Kacprzak, G. G., et al. 2013, Sci, 341, 50
Bouwens, R. J., Illingworth, G. D., Oesch, P. A., et al. 2010, ApJL, 709, L133
Cannizzo, J. K., Barthelmy, S., Cummings, J. R., Melandri, A., & de Pasquale, M. 2013, GCNR, 429
Castro, S., Galama, T. J., Harrison, F. A., et al. 2003, ApJ, 586, 128
Chen, H.-W., Perley, D. A., Pollack, L. K., et al. 2009, ApJ, 691, 152
Chen, H.-W., Perley, D. A., Wilson, C. D., et al. 2010, ApJL, 723, L218
Cooke, J., & O'Meara, J. M. 2015, ApJL, 812, L27
Cooke, J., Wolfe, A. M., Gawiser, E., & Prochaska, J. X. 2006, ApJ, 652, 994
Covino, S., Melandri, A., Salvaterra, R., et al. 2013, MNRAS, 432, 1231
Crighton, N. H. M., Murphy, M. T., Prochaska, J. X., et al. 2015, MNRAS, 452, 217
Cucchiara, A., Fumagalli, M., Rafelski, M., et al. 2015, ApJ, 804, 51
Cucchiara, A., Levan, A. J., Fox, D. B., et al. 2011, ApJ, 736, 7
da Cunha, E., Charlot, S., & Elbaz, D. 2008, MNRAS, 388, 1595
da Cunha, E., Walter, F., Smail, I. R., et al. 2015, ApJ, 806, 110
Daddi, E., Dannerbauer, H., Krips, M., et al. 2009, ApJL, 695, L176
D'Avanzo, P., Perri, M., Fugazza, D., et al. 2010, A&A, 522, A20
Davé, R., & Oppenheimer, B. D. 2007, MNRAS, 374, 427
Dawson, K. S., Schlegel, D. J., Ahn, C. P., et al. 2013, AJ, 145, 10
D'Elia, V., Fynbo, J. P. U., Goldoni, P., et al. 2014, A&A, 564, A38
Dessauges-Zavadsky, M., Calura, F., Prochaska, J. X., D'Odorico, S., & Matteucci, F. 2007, A&A, 470, 431
de Ugarte Postigo, A., Castro-Tirado, A. J., Gorosabel, J., et al. 2005, A&A, 443, 841
Eisenstein, D. J., Weinberg, D. H., Agol, E., et al. 2011, AJ, 142, 72
Elmegreen, B. G. 2015, ApJL, 814, L30
Font-Ribera, A., Miralda-Escudé, J., Arnau, E., et al. 2012, JCAP, 11, 059
Förster Schreiber, N. M., Genzel, R., Bouché, N., et al. 2009, ApJ, 706, 1364
Friis, M., De Cia, A., Krühler, T., et al. 2015, MNRAS, 451, 167
Fumagalli, M., O'Meara, J. M., Prochaska, J. X., & Kanekar, N. 2010, MNRAS, 408, 362
Fumagalli, M., O'Meara, J. M., Prochaska, J. X., Kanekar, N., & Wolfe, A. M. 2014, MNRAS, 444, 1282
Fumagalli, M., O'Meara, J. M., Prochaska, J. X., Rafelski, M., & Kanekar, N. 2015, MNRAS, 446, 3178
Fumagalli, M., O'Meara, J. M., Prochaska, J. X., & Worseck, G. 2013, ApJ, 775, 78
Fynbo, J. P. U., Gorosabel, J., Smette, A., et al. 2005, ApJ, 633, 317
Fynbo, J. P. U., Jakobsson, P., Möller, P., et al. 2003, A&A, 406, L63
Fynbo, J. P. U., Ledoux, C., Noterdaeme, P., et al. 2011, MNRAS, 413, 2481
Fynbo, J. U., Møller, P., & Warren, S. J. 1999, MNRAS, 305, 849
Gawiser, E., Francke, H., Lai, K., et al. 2007, ApJ, 671, 278
Genzel, R., Tacconi, L. J., Eisenhauer, F., et al. 2006, Natur, 442, 786
Glover, S. C. O., & Clark, P. C. 2012, MNRAS, 421, 9
Gnedin, N. Y., & Kravtsov, A. V. 2010, ApJ, 714, 287
Greiner, J., Fox, D. B., Schady, P., et al. 2015, ApJ, 809, 76
Guaita, L., Acquaviva, V., Padilla, N., et al. 2011, ApJ, 733, 114
Hibon, P., Cuby, J.-G., Willis, J., et al. 2010, A&A, 515, A97
Hjorth, J., Malesani, D., Jakobsson, P., et al. 2012, ApJ, 756, 187
Hopkins, A. M., Rao, S. M., & Turnshek, D. A. 2005, ApJ, 630, 108
Hunt, L. K., Palazzi, E., Michałowski, M. J., et al. 2014, A&A, 565, A112
Japelj, J., Vergani, S. D., Salvaterra, R., et al. 2016, A&A, 590, A129
Jimenez, R., Bowen, D. V., & Matteucci, F. 1999, ApJL, 514, L83
Jorgenson, R. A., Murphy, M. T., & Thompson, R. 2013, MNRAS, 435, 482
Jorgenson, R. A., Murphy, M. T., Thompson, R., & Carswell, R. F. 2014, MNRAS, 443, 2783
Jorgenson, R. A., & Wolfe, A. M. 2014, ApJ, 785, 16
Kann, D. A., Klose, S., & Zeh, A. 2006, ApJ, 641, 993
Kann, D. A., Klose, S., Zhang, B., et al. 2010, ApJ, 720, 1513
Kennicutt, R. C., Jr. 1998, ApJ, 498, 541
Krogager, J.-K., Fynbo, J. P. U., Møller, P., et al. 2012, MNRAS, 424, L1
Krug, H. B., Veilleux, S., Tilvi, V., et al. 2012, ApJ, 745, 122
Krühler, T., Greiner, J., Schady, P., et al. 2011, A&A, 534, A108
Krühler, T., Ledoux, C., Fynbo, J. P. U., et al. 2013, A&A, 557, A18
Krumholz, M. R. 2012, ApJ, 759, 9
Krumholz, M. R. 2013, MNRAS, 436, 2747
Krumholz, M. R. 2014, PhR, 539, 49
Krumholz, M. R., McKee, C. F., & Tumlinson, J. 2009, ApJ, 699, 850
Lanzetta, K. M., Yahata, N., Pascarelle, S., Chen, H.-W., & Fernández-Soto, A. 2002, ApJ, 570, 492
Laskar, T., Berger, E., & Chary, R.-R. 2011, arXiv:1102.1022
Madau, P. 1995, ApJ, 441, 18
Madau, P., Ferguson, H. C., Dickinson, M. E., et al. 1996, MNRAS, 283, 1388
Mawatari, K., Inoue, A. K., Kousai, K., et al. 2016, ApJ, 817, 161
McBreen, S., Krühler, T., Rau, A., et al. 2010, A&A, 516, A71
McGuire, J. T. W., Tanvir, N. R., Levan, A. J., et al. 2016, ApJ, 825, 135
Møller, P., & Warren, S. J. 1993, A&A, 270, 43
Møller, P., Warren, S. J., Fall, S. M., Fynbo, J. U., & Jakobsen, P. 2002, ApJ, 574, 51
Murphy, M. T., & Bernet, M. L. 2016, MNRAS, 455, 1043
Nagamine, K., Wolfe, A. M., Hernquist, L., & Springel, V. 2007, ApJ, 660, 945
Neeleman, M., Prochaska, J. X., Zwaan, M. A., et al. 2016, ApJL, 820, L39
Noterdaeme, P., Laursen, P., Petitjean, P., et al. 2012a, A&A, 540, A63
Noterdaeme, P., Ledoux, C., Petitjean, P., & Srianand, R. 2008, A&A, 481, 327
Noterdaeme, P., Petitjean, P., Carithers, W. C., et al. 2012b, A&A, 547, L1
Noterdaeme, P., Petitjean, P., Ledoux, C., & Srianand, R. 2009, A&A, 505, 1087
Noterdaeme, P., Petitjean, P., Pâris, I., et al. 2014, A&A, 566, A24
Oesch, P. A., Bouwens, R. J., Illingworth, G. D., et al. 2012, ApJ, 759, 135
Oke, J. B., & Gunn, J. E. 1983, ApJ, 266, 713
O'Meara, J. M., Chen, H.-W., & Kaplan, D. L. 2006, ApJL, 642, L9
O'Meara, J. M., Prochaska, J. X., Burles, S., et al. 2007, ApJ, 656, 666
O'Meara, J. M., Prochaska, J. X., Worseck, G., Chen, H.-W., & Madau, P. 2013, ApJ, 765, 137
Perley, D. A., Cenko, S. B., Bloom, J. S., et al. 2009, AJ, 138, 1690
Perley, D. A., Levan, A. J., Tanvir, N. R., et al. 2013, ApJ, 778, 128
Perley, D. A., Morgan, A. N., Updike, A., et al. 2011, AJ, 141, 36
Perley, D. A., Tanvir, N. R., Hjorth, J., et al. 2016, ApJ, 817, 8
Péroux, C., Bouché, N., Kulkarni, V. P., York, D. G., & Vladilo, G. 2012, MNRAS, 419, 3060
Péroux, C., McMahon, R. G., Storrie-Lombardi, L. J., & Irwin, M. J. 2003, MNRAS, 346, 1103

Péroux, C., Quiret, S., Rahmani, H., et al. 2016, MNRAS, 457, 903
Prochaska, J. X., Chen, H.-W., Dessauges-Zavadsky, M., & Bloom, J. S. 2007, ApJ, 666, 267
Prochaska, J. X., Herbert-Fort, S., & Wolfe, A. M. 2005, ApJ, 635, 123
Prochaska, J. X., O'Meara, J. M., & Worseck, G. 2010, ApJ, 718, 392
Prochaska, J. X., Sheffer, Y., Perley, D. A., et al. 2009, ApJL, 691, L27
Prochaska, J. X., & Wolfe, A. M. 1997, ApJ, 487, 73
Prochaska, J. X., & Wolfe, A. M. 2009, ApJ, 696, 1543
Rafelski, M., Gardner, J. P., Fumagalli, M., et al. 2016, ApJ, 825, 87
Rafelski, M., Neeleman, M., Fumagalli, M., Wolfe, A. M., & Prochaska, J. X. 2014, ApJL, 782, L29
Rafelski, M., Wolfe, A. M., & Chen, H.-W. 2011, ApJ, 736, 48
Rafelski, M., Wolfe, A. M., Prochaska, J. X., Neeleman, M., & Mendez, A. J. 2012, ApJ, 755, 89
Rahmati, A., & Schaye, J. 2014, MNRAS, 438, 529
Rahmati, A., Schaye, J., Bower, R. G., et al. 2015, MNRAS, 452, 2034
Rahmati, A., Schaye, J., Crain, R. A., et al. 2016, MNRAS, 459, 310
Ribaudo, J., Lehner, N., & Howk, J. C. 2011, ApJ, 736, 42
Salvaterra, R., Della Valle, M., Campana, S., et al. 2009, Natur, 461, 1258
Savaglio, S., Glazebrook, K., & Le Borgne, D. 2009, ApJ, 691, 182
Schady, P., Dwelly, T., Page, M. J., et al. 2012, A&A, 537, A15
Schlafly, E. F., & Finkbeiner, D. P. 2011, ApJ, 737, 103
Schmidt, M. 1959, ApJ, 129, 243
Schulze, S., Fynbo, J. P. U., Milvang-Jensen, B., et al. 2012, A&A, 546, A20
Sparre, M., Hartoog, O. E., Krühler, T., et al. 2014, ApJ, 785, 150
Srianand, R., Hussain, T., Noterdaeme, P., et al. 2016, MNRAS, 460, 634
Stanway, E. R., Levan, A. J., Tanvir, N. R., Wiersema, K., & van der Laan, T. P. R. 2015, ApJL, 798, L7
Steidel, C. C., Giavalisco, M., Dickinson, M., & Adelberger, K. L. 1996, AJ, 112, 352
Storrie-Lombardi, L. J., & Wolfe, A. M. 2000, ApJ, 543, 552
Tanvir, N. R., Fox, D. B., Levan, A. J., et al. 2009, Natur, 461, 1254
Thöne, C. C., Campana, S., Lazzati, D., et al. 2011, MNRAS, 414, 479
Thöne, C. C., Fynbo, J. P. U., Goldoni, P., et al. 2013, MNRAS, 428, 3590
Tilvi, V., Rhoads, J. E., Hibon, P., et al. 2010, ApJ, 721, 1853
Tyson, N. D. 1988, ApJL, 329, L57
Wang, W.-H., Chen, H.-W., & Huang, K.-Y. 2012, ApJL, 761, L32
Weatherley, S. J., Warren, S. J., Møller, P., et al. 2005, MNRAS, 358, 985
Wolfe, A. M., & Chen, H.-W. 2006, ApJ, 652, 981
Wolfe, A. M., Gawiser, E., & Prochaska, J. X. 2005, ARA&A, 43, 861
Wolfe, A. M., & Prochaska, J. X. 1998, ApJL, 494, L15
Wolfire, M. G., McKee, C. F., Hollenbach, D., & Tielens, A. G. G. M. 2003, ApJ, 587, 278
Woosley, S. E., & Bloom, J. S. 2006, ARA&A, 44, 507
Zafar, T., Péroux, C., Popping, A., et al. 2013, A&A, 556, A141
Zafar, T., Watson, D., Fynbo, J. P. U., et al. 2011, A&A, 532, A143
Zafar, T., Watson, D. J., Malesani, D., et al. 2010, A&A, 515, A94
Zwaan, M. A., & Prochaska, J. X. 2006, ApJ, 643, 675